Image Reconstruction Analysis for Positron Emission Tomography with Heterostructured Scintillators

Philipp Mohr, Nikos Efthimiou, *Member, IEEE,* Fiammetta Pagano, Nicolaus Kratochwil, Marco Pizzichemi, Charalampos Tsoumpas, *Senior Member, IEEE,* Etiennette Auffray, *Member, IEEE,* and Karl Ziemons, *Member, IEEE*

***Abstract*—The concept of *structure engineering* has been proposed for the exploration of the next generation of radiation detectors with improved performance. A Time Of Flight Positron Emission Tomography (TOF-PET) scanner with heterostructured scintillators with a pixel size of $3.0\times3.1\times15$ mm^3 was simulated. The heterostructures consisted of alternating layers of BGO as a dense material with high stopping power and plastic as a fast light emitter. Using the GATE simulation toolkit, a detector time resolution was calculated as a function of the deposited and shared energy in both materials on an event-by-event basis. We saw that while sensitivity was reduced to 32% for 100 μm thick plastic layers and 52% for 50 μm, the CTR distribution improved to 204 ± 49 ps and 220 ± 41 ps respectively, compared to 276 ± 9 ps for bulk BGO. We divided the events into three groups based on their CTR and modeled them with different Gaussian TOF kernels. On a NEMA IQ phantom, the heterostructures had better contrast recovery in early iterations, while on the other hand, BGO achieved a better Contrast-to-Noise Ratio (CNR) after the 10th - 15th iteration due to the higher sensitivity. The developed simulation and reconstruction methods constitute new tools for evaluating different detector designs with complex time responses.**

***Index Terms*—TOF PET, Heterostructure, Metascintillator, Multiple TOF kernels**

This work did not involve human subjects or animals in its research.

N. Efthimiou was supported in part by NIH grants R21-CA239177, R01-EB028764, R01-CA196528, R01-CA113941. C. Tsoumpas was sponsored in part by a Royal Society Industry Fellowship (IF170011).

Philipp Mohr was with FH Aachen University of Applied Sciences, Jülich, Germany. He is now with the Department of Nuclear Medicine and Molecular Imaging, University Medical Center Groningen, Groningen, Netherlands (contact: p.mohr@umcg.nl).

Nikos Efthimiou is with the Department Radiology, Perelman School of Medicine, University of Pennsylvania, USA.

Fiammetta Pagano and Marco Pizzichemi are with University of Milano-Bicocca, Milano, Italy, and with European Organization for Nuclear Research, Geneve, Switzerland (CERN).

Nicolaus Kratochwil is with European Organization for Nuclear Research, Geneve, Switzerland (CERN) and with University of Vienna, Vienna, Austria.

Charalampos Tsoumpas is with the Department of Nuclear Medicine and Molecular Imaging, University Medical Center Groningen, University of Groningen, Groningen, Netherlands and with the Biomedical Imaging Science Department, Leeds Institute of Cardiovascular and Metabolic Medicine, University of Leeds, Leeds, UK.

Etiennette Auffray is with European Organization for Nuclear Research, Geneve, Switzerland (CERN).

Karl Ziemons is with FH Aachen University of Applied Sciences, Jülich, Germany.

I. Introduction

Positron Emission Tomography (PET) is a highly sensitive imaging modality in nuclear medicine that reveals the metabolic or biochemical functions of tissues and organs. PET is able to image many cellular pathways of receptors, providing global and regional assessments of diseases. The scanner detects pairs of 511 keV gamma rays emitted from electron-positron annihilations propagating along a Line Of Response (LOR) [1].

Arguably, the two driving factors for the sensitivity of a PET system are the scanner's geometry and the stopping power of the detector's scintillating material. Inorganic scintillators with high density and effective atomic number like Cerium doped Lutetium Oxyorthosilicate (LSO/LYSO) or Bismuth Germanate (BGO) are commonly used due to their high gamma ray stopping power [2]. Another important requirement for modern PET scanners is to exhibit very good Coincidence Time Resolution (CTR), since by measuring the detection time difference between the two gamma rays we can restrict the likelihood of the annihilation's position along the LOR; this is known as TOF [3]. It has been proven, that improving the CTR increases the Signal to Noise Ratio (SNR) gain in the reconstructed images [4] and even has the potential to overcome the limitations induced by the physical size of detectors on spatial resolution [5]. TOF offers significantly better image quality which can be translated to shorter acquisition time or lower injected doses [6]–[11]. Nowadays, the CTR of commercially available PET scanners is in the range of 200–300 ps [12], [13].

The chief advantage of inorganic scintillators is their high stopping power for 511 keV gamma rays. On the other hand, organic scintillators have better CTR for PET [14], [15], but lower density and effective atomic number; thus, their low stopping power is a severe drawback for their wide adoption.

Heterostructured scintillators attempt to alleviate the natural limitations of the above types of scintillators by combining them in one detector pixel with only the advantageous properties. These next-generation scintillation detectors apply the concept of structure engineering [16]–[18]. For heterostructured scintillators, the basic idea is that the gamma ray is stopped by the dense inorganic scintillator, while the recoil electron deposits some of its energy in the fast organic material, resulting in better overall timing resolution. In lit-

erature, the term metascintillator has been used to describe heterostructured scintillators [19], picking up the concept of metamaterials in material science. These heterostructured scintillators take a step forward in the improvement of time resolution as sought by the 10 ps challenge [20].

An experimental proof-of-concept for a heterostructured scintillator has been presented in [21] with $3.8 \times 3.8 \times 3$ mm^3 pixels of 200 μm thick layers of alternating BGO or LYSO with a fast plastic scintillator. The authors identified different types of events with standard CTR of the bulk material or improved CTR due to energy deposition in the fast emitter. In follow-up work, Pagano *et al.* [22] investigated a similar design for longer crystals $3 \times 3 \times 15$ mm^3 and different layer thicknesses. Lecoq *et al.* [23] also report results on LYSO and BGO-based heterostructures. Both works mention that the layers of the heterostructure should be smaller than the recoil range of the electrons to allow energy sharing between the two materials. In BGO, the average range of the primary electrons generated by 511 keV gamma rays is below 100 μm, whereas for LYSO it is slightly above 100 μm [24], [25].

Recently, Krause *et al.* [26] based on Monte Carlo simulations of different heterostructure configurations, proposed a set of guidelines for designing heterostructures. The authors stress the importance of maximizing the fraction of fully absorbed events, possibly by increasing the detectors' length and increasing the fast material's thickness to facilitate energy sharing. The authors discussed the various contradictions they faced, and we will also be discussing them in later paragraphs of this paper.

In this paper, we investigated the potential impact of combining a dense, inorganic scintillator with a fast, organic scintillator on PET imaging and image quality. For each registered event, the time resolution depends on the energy deposition to each material, especially to the fast scintillator. This leads to an interesting trade-off. On the one hand, a larger volume fraction of the organic material in the heterostructured scintillator improves the CTR, while on the other hand, it also decreases the stopping power. Predicting the impact of the volume fraction and the sampling frequency (number of layers) is not trivial, and we used Monte Carlo simulations for two example BGO/plastic heterostructured scintillators to that end. In addition, in the image reconstruction, we exploited the fraction of events with a faster CTR by applying different timing kernels [27]. We compare the performance of a heterostructure-based scanner to one with bulk BGO detectors in terms of count rates and the quality of the reconstructed images in terms of contrast recovery (CRC) and contrast to noise ratio (CNR) using the NEMA IQ phantom.

II. Materials and Methods

A. Time Resolution Function for Heterostructured Scintillators

In this work, we implemented a function for the calculation of the time resolution of each event in the simulation. This function accounts for the energy sharing-dependent time resolution of the heterostructured scintillators.

Typically, in PET, the time resolution is assumed to be the same for the two detectors ([28]) and the relationship between Detector Time Resolution (DTR) and CTR is given by $CTR = \sqrt{2} \cdot DTR$. However, for the general case where the two detectors may have different time resolutions, the CTR is expressed as $CTR = \sqrt{DTR_1^2 + DTR_2^2}$, where DTR_1 and DTR_2 are the time resolutions of the two detectors involved in the coincidence.

In heterostructures, the DTR is a function of energy deposition in both materials, which is a statistical process; therefore, in general the time response of the two detectors can be different.

The model of the energy-dependent DTR ($DTR(E)$) is proportional to the inverse of the square root of the initial photon-time density (IPTD), which is, in turn, proportional to the energy-dependent intrinsic light yield [29], [30]:

$$DTR(E) = \frac{1}{\sqrt{IPTD(E)}} \tag{1}$$

$$IPTD(E) = \frac{ILY(E)}{\tau_{deff}(1.57\tau_r + 1.13\sigma_{SPTR+PTS})} \tag{2}$$

where τ_{deff} is the effective decay time, τ_r the scintillation rise time, ILY the intrinsic light yield, and $\sigma_{SPTR+PTS}$ combines the contribution due to the Single Photon Time Resolution (SPTR) of the Silicon Photomultiplier (SiPM) and the photon transfer time spread. This empirical equation has been established by Vinogradov [29]. Gundacker *et al.* [30] showed that it provides a good estimate of the measured time resolution of scintillators with high-frequency readout.

The novelty of heterostructure scintillators is that the time resolution is a function of the energy deposition in two materials. The idea is that the IPTDs of the individual materials can be added to determine the combined time resolution:

$$DTR(E_{Pl}, E_{BGO}) = \frac{1}{\sqrt{IPTD_{Pl}(E_{Pl}) + IPTD_{BGO}(E_{BGO})}} \tag{3}$$

Since the individual IPTDs are proportional to the energy deposited in the specific material, we can calculate them as:

$$IPTD_{Pl}(E_{Pl}) = \frac{E_{Pl}/340}{DTR^2_{Pl@340keV}} \tag{4}$$

$$IPTD_{BGO}(E_{BGO}) = \frac{E_{BGO}/511}{DTR^2_{BGO@511keV}} \tag{5}$$

where we used the time resolutions measured with the individual bulk materials and normalize the deposited energies to the reference energies of the Compton edge for the plastic scintillator and the photopeak (511 keV) for BGO. The time resolutions of the individual bulk materials were measured for a geometry of $3\times3\times15$ mm^3 with the same setup as previously described in [30]. The scintillators were wrapped in Teflon and coupled to the photodetector using Meltmount.

With $3 \times 3 \times 15$ mm^3 scintillator pixels, we measured CTRs of 271 ps for BGO and 94 ps for the plastic EJ232 (Eljen Technology) at 511- and 340 keV, respectively. Based on the above measurements, we calculated $DTR_{Pl@340keV}$ and $DTR_{BGO@511keV}$ as described previously.

It has to be noted that the model we used here is a simple approximation and does not consider effects due to the thin plate-shaped structure such as different light transport and stronger Depth Of Interaction (DOI) bias. In fact, we have treated the DOI impact similar to the DOI of normal 15 mm crystals, which we will describe in section II-C. To summarize, our model serves as a simple method to calculate the CTR on an event-by-event basis and study the influence of the resulting CTR distribution on the reconstructed image.

Furthermore, we acknowledge that the input values ($DTR_{Pl@340keV}$ and $DTR_{BGO@511keV}$) come from laboratory measurements with optimized conditions regarding readout electronics, data acquisition, and analysis on single pixels.

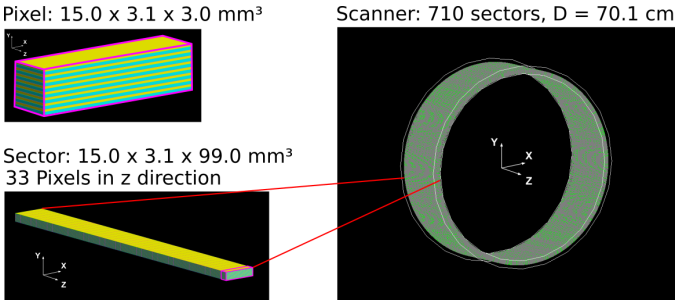

Fig. 1. (Top left) a single BGO/plastic heterostructured scintillator is demonstrated. (Bottom left) The single heterostructure was repeated on the axial direction to create the scanner's modules. (Right) the entire cylindrical scanner is shown after repeating the sector with the GATE ring repeater, is shown.

B. Monte Carlo Simulations

We performed Monte Carlo simulations using a modified GATE simulation toolkit (v8.2) [31]. Simulations provide insight into the fractions of energy deposited in plastic and BGO layers enabling an understanding of energy sharing between the two materials the resulting DTR. We implemented the $DTR(E_{Pl}, E_{BGO})$ function in the readout module (`GateReadout` class), where we sum separately the energies deposited in the BGO and plastic layers and use them to generate a final output pulse with a DTR as described in Eq. 3, that varies on an event-by-event basis.

We simulated a cylindrical PET geometry with a diameter of 701.0 mm and an axial length of 99.0 mm. The system consisted of 33 detector rings each with 710 detectors with size $3.0 \times 3.1 \times 15.0$ mm^3. This arrangement led to a PET geometry as close to a cylinder as possible, avoiding gaps. We kept axial length below 10 cm to keep the computational effort required for simulation and reconstruction at reasonable levels.

Each heterostructured scintillator consists of a stacking of alternating BGO and plastic layers along the transaxial direction (Fig. 1). In this study, two heterostructure models were investigated; one with, equal, 100 μm BGO and plastic layers (31 layers in total) and one with 100 μm BGO and 50 μm plastic layers (41 in total). For simplicity, these two geometries will be referred to as Hetero-Pl-100 and Hetero-Pl-50 throughout the paper. In order to reduce the effect of energy escaping the detector, all heterostructures started and ended with a BGO layer. We fixed the thickness of 100 μm for BGO based on the range of recoil electrons in BGO [25] and to be close to what is used experimentally by Pagano *et al.* [22]. By choosing 100 μm and 50 μm plastic layers, the sensitivity of LYSO is between the sensitivity of these two configurations (as shown later in Fig. 5). Our reference model was based on bulk BGO crystals of $3.0 \times 3.1 \times 15$ mm^3 and was simulated with the same energy-dependent DTR model.

The Geant4 physics list was set to `emstandard_opt3` with an additional reduction of the production cuts from the default 1 mm to 5 μm in the detector volumes to allow a more accurate simulation of the energy distribution between the thin layers of 50 and 100 μm.

We have to note that the simulations record the energy deposition from each gamma ray in the two materials, and optical photons were not simulated. The deposited energies were input to the DTR function based on experimental measurements.

The coincidence window was set to 4 ns and the GATE parameter `minSectorDifference` to 88 [32]. In previous work on TOF PET reconstruction applied on Cherenkov radiation in BGO [27], energy resolution of 19% was measured, whereas, for the heterostructured scintillators, worse resolution can be expected due to the layered structure. Here, to isolate the effects of CTR on the reconstruction of TOF PET image reconstruction, the same energy resolution 20% and an energy window of $400 - 650$ keV were used in all models.

We simulated the geometry of a typical NEMA Image Quality (IQ) phantom [33] with four hot spheres (diameters 10-, 13-, 17-, and 22 mm) and two cold spheres (28- and 37 mm). The background activity was 42.9 MBq and the hot sphere ratio was 4:1. The duration of the simulated acquisitions were 2000 s.

C. Photon Travel Spread in the Simulations

As shown in Eq. 2, the Photon Time Spread (PTS) (similar to the DOI error, but in terms of time) affects the simulated time resolution's width and shape [32]. The PTS is caused by the natural uncertainty in the gamma ray's absorption point inside the crystal; thus, its contribution cannot be ignored during the simulation. Therefore the input DTRs values ($DTR_{Pl@340keV}$ and $DTR_{BGO@511keV}$) have to be pre-corrected for PTS in order to get at the output the desired CTR. To roughly estimate the CTR without PTS (denoted as CTR$'$), we simulated a point source and fitted a Gaussian function on the time differences of the timestamps of photoelectric absorption of the two events in coincidence. We found a FWHM of 51 ps and subtracted it from the target CTR in quadrature. The simulated PTS value of 51 ps is very close to the empirical value of 50 ps that corresponds to the crystal's length divided by the speed of light, per the observation made in [34], where this empirical formula has been shown to work for LSO crystals.

In Table I, we summarize the information on the simulated time resolutions. In the first column, we specify the target CTR that we aim to achieve at the end of the simulation. The second column shows the CTR after correction for PTS; this is an intermediate value that we use to calculate the DTR.

TABLE I
TARGETED CTR FOR THE SIMULATION OUTPUT. TIME RESOLUTIONS CORRECTED FOR THE NATURAL PHOTON TRAVEL SPREAD AND DETECTOR TIME RESOLUTIONS USED TO OBTAIN THE TARGET CTRS. THREE DIFFERENT INPUT TIME RESOLUTIONS ($DTR_{Pl@340keV}$) WERE CONSIDERED: PL-τ1, PL-τ2 AND PL-τ3.

	CTR (ps)	CTR′ (ps) $^{\alpha}$	DTR (ps) $^{\beta}$
BGO	271	266.2	188.2
Pl-τ1	94	79.0	55.9
Pl-τ2	75	55.0	38.9
Pl-τ3	51	0	0

$^{\alpha}\, CTR' = \sqrt{CTR^2 - PTS^2}$
$^{\beta}\, DTR = CTR'/\sqrt{2}$

Finally, in the third column, we show the $DTR_{Pl@340keV}$ and $DTR_{BGO@511keV}$ as per Eq. 4&5 that we used to obtain the targeted CTRs. We simulated three different input time resolutions for plastic ($DTR_{Pl@340keV}$). These include the experimental value of Pl-τ1 $=$ 94 ps, and two faster resolutions: Pl-τ2 $=$ 75 ps and Pl-τ3 $=$ 51 ps. With the faster resolutions, the influence of having a material with higher IPTD and similar density of plastic is investigated.

D. Image Reconstruction

We reconstructed the data with the TOF LM-MLEM, as implemented in the open source image reconstruction toolkit Software for Tomographic Image Reconstruction (STIR) [34]–[36]. We excluded random and scattered events identified by the GATE simulation, thus only reconstructing trues. The data were sorted in 355 views $\times$351 tangential positions over 33 segments. The timing differences were discretized in 1 ps bins, with an integration size of 0.149 mm. An odd number of TOF bins was used to get a centered TOF bin.

The voxel size of the reconstructed images was $2 \times 2 \times 1.5$ mm^3 on $160 \times 160 \times 65$ grid. All configurations were reconstructed for 100 iterations and a Gaussian filter with FWHM 3 mm^3 was applied post-reconstruction.

We calculated the attenuation correction analytically with the phantom's linear attenuation values, found in NIST [37]. For the calculation of the normalization factors we simulated a cylindrical back-to-back source with a diameter of 660 mm, covering the entire Field Of View (FOV) without any attenuation. The simulations collected over 10^9 events for each detector configuration.

In Fig. 2 we show the CTR′ distributions (without PTS) for all simulated data sets. As one can see, the BGO events are clustered around a single peak. On the other hand, the heterostructures have three peaks in their distributions. Each peak corresponds to different combinations between detectors 1 and 2. The first peak contains shared events on both detectors (fast-fast). In the second peak, energy sharing took place in one of the two detectors (fast-slow), and in the third peak, we had BGO-only interactions (slow-slow). The shape of the peaks depends on the input time resolutions, and we see that they are better separated with faster plastic (Pl-τ3 compared to Pl-τ1).

To simplify the reconstruction model, we divided the CTR values into three groups (g) to use three Gaussian timing

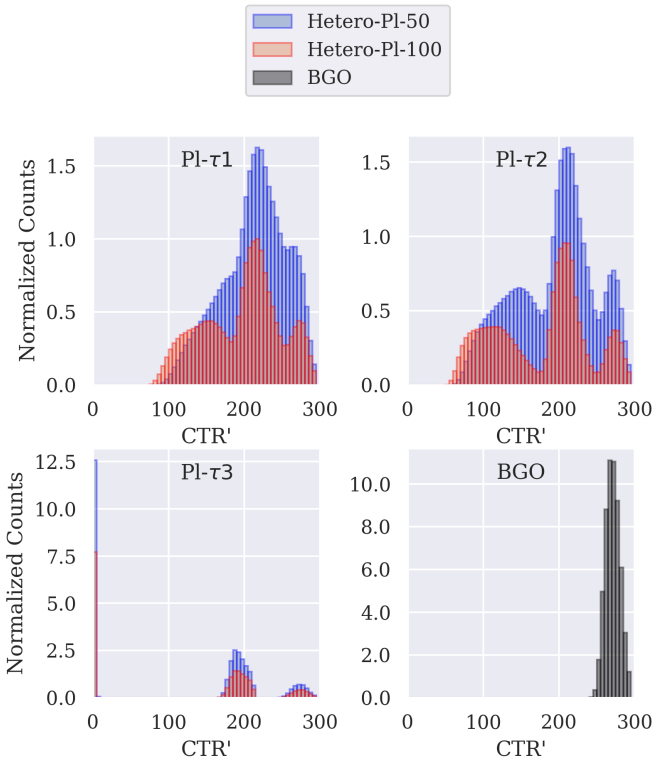

Fig. 2. CTR′ distributions for all simulated data sets with input resolutions as given in Table I. Three peaks can be clearly distinguished for the heterostructure configurations. For visualization purposes, the counts were normalized to the amplitude in the second group of the Hetero-Pl-100-τ1 configurations.

kernels. For the Pl-τ1 and Pl-τ2 cases, we applied constant thresholds at 175- and 250 ps, respectively. For Pl-τ3, we reduced these thresholds to ensure that all events in the clearly separated groups in Fig. 2 (bottom left) get processed in their corresponding kernel. For each group (g), the TOF kernel (f_g) width in the reconstruction was the unweighted arithmetic mean $\overline{CTR'}_g$ of the applied resolutions inside the boundaries. However, as discussed in par. II-C, to avoid underestimating the width of the TOF kernel, we added in quadrature the PTS:

$$f_g = \sqrt{\overline{CTR'}_g^2 + PTS^2} \tag{6}$$

We present all resulting $\overline{CTR'}_g$ and f_g values in Table II, as well as the proportion of each group as a percentage of the total number of events.

E. Figures of Merit

In this study, we used the CRC and CNR. For the hot spheres, the CRC is calculated as:

$$CRC_r = \frac{\left(\frac{\mu_{H,d}}{\mu_{B,d}} - 1\right)}{\alpha - 1} \cdot 100\% \tag{7}$$

where μ_H is the mean value in a spherical region of interest (ROI) with diameter d, that of the respective sphere (r), μ_B is the mean value in the background taken using 24 circular

TABLE II
AVERAGE CTR′ PER GROUP($\overline{CTR'}_g$), THE CORRESPONDING FHWM OF THE TOF KERNEL USED IN THE RECONSTRUCTION (fg) AND THE (%) PROPORTION OF EACH GROUP FOR BOTH HETEROSTRUCTURES (HETERO-PL-50 AND HETERO-PL-100), THE THREE SIMULATED TIME RESOLUTIONS FOR THE PLASTIC LAYER AND BGO.

Group	$\overline{CTR'}_g(ps)$ [α]	f_g (ps) [β]	Proportion (%)
Hetero-Pl-50			
		Pl-τ1	
1	147.4	155.9	19.6
2	215.6	221.5	59.3
3	267.9	272.7	21.1
		Pl-τ2	
1	130.8	140.4	33.3
2	212.6	218.7	51.1
3	270.5	275.3	15.6
		Pl-τ3	
1	1.2	51.0	41.7
2	193.1	199.7	45.8
3	273.2	277.9	12.6
Hetero-Pl-100			
		Pl-τ1	
1	139.2	148.2	35.3
2	216.6	222.6	50.8
3	272.9	277.6	14.0
		Pl-τ2	
1	112.4	123.5	40.5
2	209.5	215.7	46.5
3	273.3	278.1	13.0
		Pl-τ3	
1	0.8	51.0	42.2
2	193.7	200.3	45.5
3	274.1	278.8	12.3
BGO			
1	271.2	275.9	100.0

[α] Mean CTR′ of group (FWHM)
[β] $f_g = \sqrt{\overline{CTR'}^2_{group} + PTS^2}$

ROIs in the two central slices and α is the true activity ratio, which is 4 in this case.

The CNR is given by:

$$CNR = \frac{\mu_{H,d} - \mu_{B,d}}{\sqrt{\sigma^2_{H,d} + \sigma^2_{B,d}}} \tag{8}$$

where σ_H and σ_B is the standard deviation in the hot sphere and background, respectively.

III. RESULTS

A. Time Resolution as Function of Energy Sharing

In Fig. 3, we show the response of $DTR(E_{BGO}, E_{Pl})$ as a function of E_{Pl} from the initial energy of 511 keV. We also visualize the individual contributions of the energies deposited in each material to the combined CTR by setting either $E_{BGO} = 0$ or $E_{Pl} = 0$ in Eq. 3. By doing so, "BGO only" and "Plastic only" show the time resolution based only on E_{BGO} or E_{Pl}.

We see in the curves of Fig. 3 that the DTR of BGO layers gets progressively worse as more energy is deposited in the plastic, whereas the DTR based solely on E_{Pl} ("plastic only") improves continuously.

As demonstrated by the curves of "combined DTR" and "combined CTR", the time resolution of the heterostructured scintillator improves as more energy is absorbed in the plastic layers.

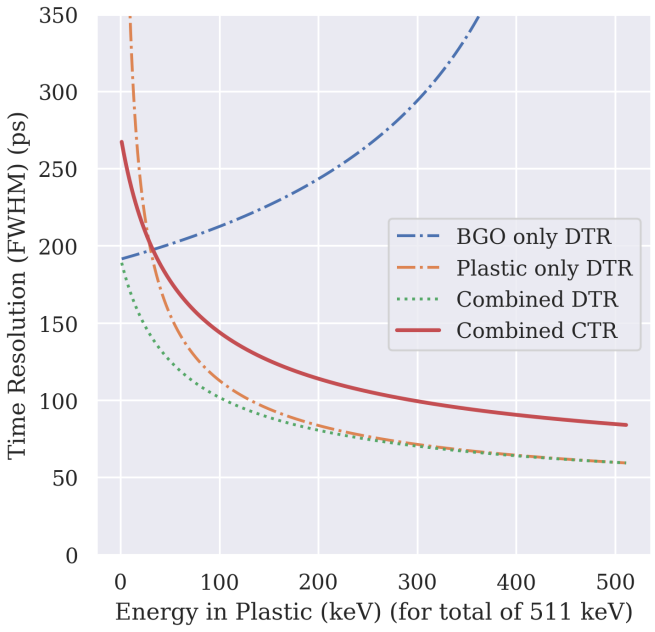

Fig. 3. Analytically calculated time resolution as function of the energy in plastic for a total of 511 keV with CTR input values of 271 ps for BGO and 94 ps for plastic. Shown are the individual DTRs of both materials and the combined resolution expressed as DTR and CTR, assuming the same energy was deposited in both detector pairs ($CTR = \sqrt{2} \cdot DTR$). With increasing energy in plastic, the faster plastic scintillator dominates the time resolution.

Finally, we see that when the energy deposited in the plastic exceeds the 300 keV, the combined DTR is nearly the same as the "plastic only" case, which indicates that the fast photons drive the CTR values.

In Fig. 4 the energy distribution of the shared events ($E_{Pl} > 0\,\text{keV}$) of Hetero-Pl-100 geometry, is shown, based on an acquisition of 2000 s resulting in 49.8×10^6 coincidences. In this case, the shared events account for 63.5% of the total. The rest deposit their energy only in BGO. It can be observed that most of the shared events deposit only a low fraction of their energy in the plastic. The fraction of events with energy in the plastic above $50\,\text{keV}$ is 43.1%. In case of the Hetero-Pl-50 geometry, recording 82.9×10^6 coincidences, the simulations showed 63.0% shared events and 29.6% exceeding $50\,\text{keV}$.

For the two configurations in this work, the fraction of shared events remains about the same (driven by the $100\ \mu\text{m}$ BGO thickness), but the fraction of events with more than 50 keV deposited in plastic is higher for the thicker plastic layers. For instance, the average deposited energy and standard deviation is 108.4 ± 83.4 keV and 65.7 ± 60.1 keV for Hetero-Pl-100 and Hetero-Pl-50, respectively.

B. Time Resolution Over Sensitivity

In Fig. 5, we show box plots of the CTR distributions for the Heterostructure configurations with the experimental value of Pl-τ1 = 94 ps and for the two bulk scintillators BGO and LYSO. On the x-axis, we show the drop in the count rate compared to BGO.

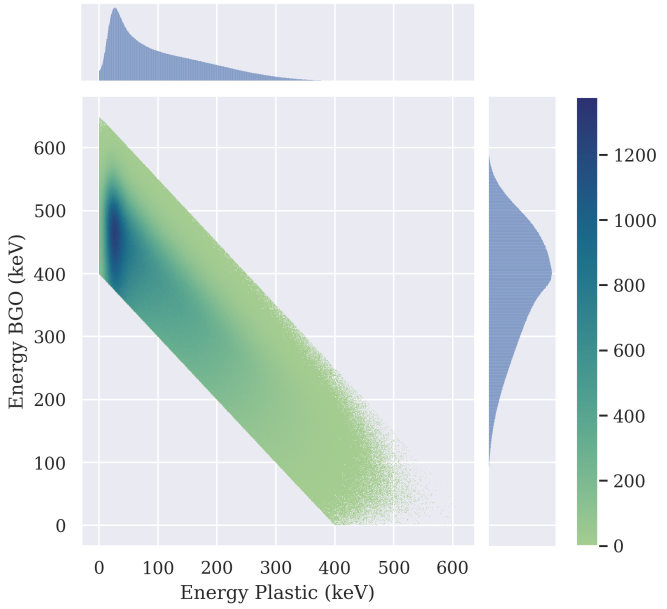

Fig. 4. Energy distribution between both materials of Hetero-Pl-100 geometry. Only shared events are shown.

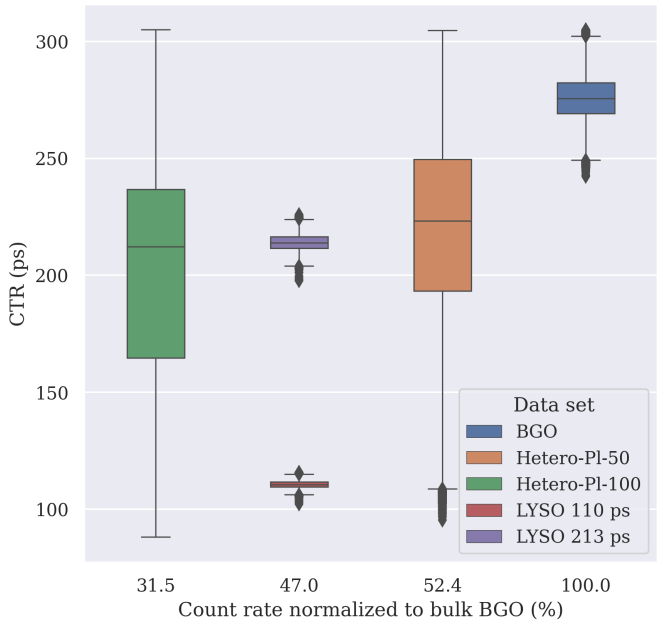

Fig. 5. CTR vs true coincidence rate normalised to bulk BGO for different scanner configurations. $400-650$ keV energy window and 20% resolution for BGO and Heterostructure, $450-650$ keV energy window and 11 % resolution for LYSO. For this study, an equivalent CTR for the of 271 ps for BGO and 94 ps for plastic was simulated. For LYSO, the value 213 ps represents the Siemens Vision PET scanner and 110 ps was approximated for LYSO under laboratory conditions based on [30].

TABLE III
AMOUNT OF COINCIDENCES REGISTERED IN THE NEMA IQ SIMULATIONS.

	Hetero-Pl-100	Hetero-Pl-50	BGO
Prompts	49.8×10^6	82.9×10^6	158.0×10^6
Trues	27.9×10^6	46.3×10^6	88.4×10^6

As it can be seen, the use of thicker plastic layers leads to improved CTR; however, it also results in a noticeable reduction in the count rate to 31.5% of BGO's. While with thinner plastic layers, the value is 52.4%. The CTR distributions show mean and standard deviation of 204 ± 49 ps, 220 ± 41 ps, 276 ± 9 ps for Hetero-Pl-100, Hetero-Pl-50 and bulk BGO, respectively. It should be noted that the CTR distributions of heterostructures show a spread of values between approximately 100 and 300 ps. Considerably higher than bulk materials.

For comparison, we included simulations of LYSO detectors with input CTRs of 213- (Siemens Biograph vision [12]) and 110 ps (laboratory conditions [30]). We see that the count rate of LYSO falls in-between the two heterostructure configurations with a coincidence rate of 47.0% that of BGO and resulted in a CTR of 214 ± 4 ps and 111 ± 2 ps for an energy threshold of 450 keV and 11% energy resolution.

C. Image Quality

We summarize basic statistics on the NEMA IQ simulated data sets used in reconstruction in Table III. The measured drop in true counts was 32% and 52% for Hetero-Pl-100 and Hetero-Pl-50, respectively.

In Fig. 6, we shown the images obtained at the 60^{th} iteration for all simulated scanner models. Due to the drop in stopping power and disproportional improvement in the time resolution, we can see in the images higher noise when thicker plastic layers are used.

The coefficient of variation (CoV) at the background is 2%, 2.5% and 3.6% for the BGO, Pl-50-$\tau 1$ and Pl-100-τ_1 images, respectively. However, it is not possible to directly compare the CoV between the three images as they have been reconstructed with different time resolutions; thus, MLEM has converged at different rates. We see that with 75 ps plastic time resolution (Pl-$\tau 2$), the CoV is 2.7% and 3.6% for the Pl-50 and Pl-100, which shows that convergence can further speed up using faster plastic with thinner layers, while there may be no additional benefit for the case of Pl-100. The above suggests that even if the input time resolution of the material improves, the perceived TOF effect still depends on the average deposited energy in the plastic.

In Fig. 7 we show the CRC for the BGO and Hetero-Pl-100 with the three plastic time resolutions. For the 22-, 17- and 13 mm spheres, the heterostructure has a slightly faster convergence than BGO, which is more pronounced in the earlier ($<$15 iterations). This improvement comes from the better CTR distribution. Also, as the CoV suggests, we do not see a marked difference between 94 ps (Pl-$\tau 1$) and 75 ps (Pl-$\tau 2$).

Furthermore, we see that the 51 ps plastic loses contrast because, in this case, the shape of the timing spread heavily depends on the DOI, and thus the TOF modeling with a single Gaussian function is not appropriate [32].

In terms of CNR (Fig. 8), BGO has the best performance, followed by Hetero-Pl-50 and Hetero-Pl-100. The above was expected [38], as the three models produce images with

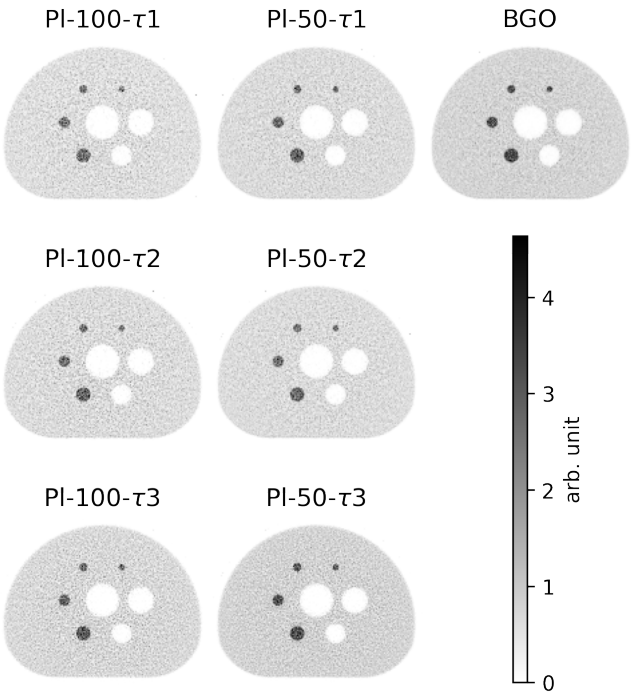

Fig. 6. Reconstructed images at the 60^{th} iteration for three scanner configurations Hetero-Pl-100, Hetero-Pl-50 and BGO and for three different plastic time resolutions: Pl-τ1 = 94 ps, Pl-τ2 = 75 ps and Pl-τ3 = 51 ps.

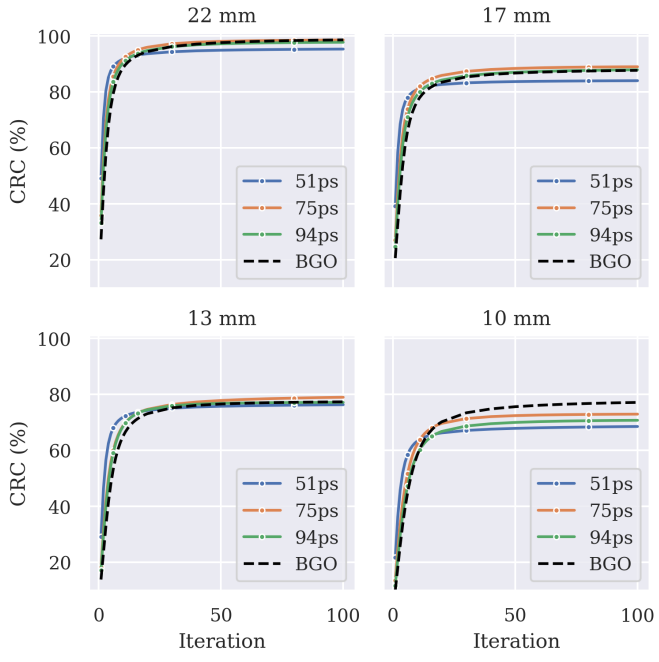

Fig. 7. Contrast recovery coefficient of the four hot spheres of the NEMA IQ phantom, for the BGO (271 ps) and the Hetero-Pl-100 geometry, with $Pl-\tau1 = 94$ ps, $Pl-\tau2 = 75$ ps and $Pl-\tau3 = 51$ ps. Similar curves were obtained for the Hetero-Pl-50 geometry.

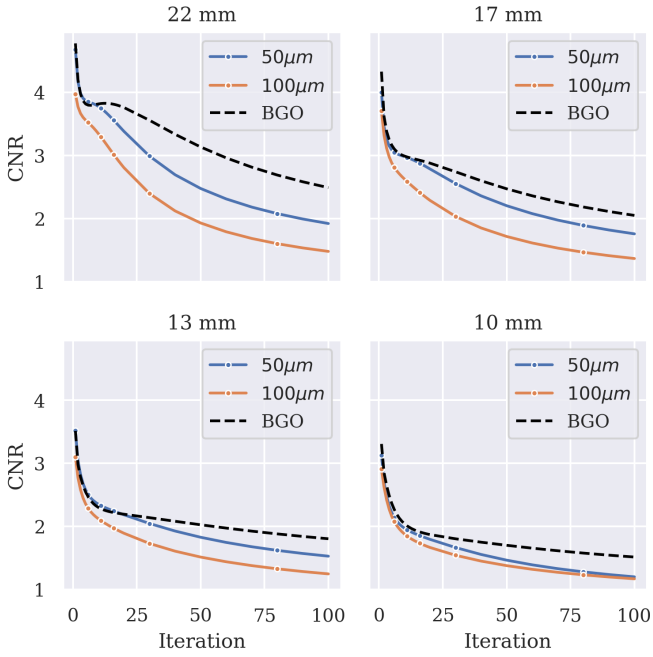

Fig. 8. Contrast-to-Noise ratio for BGO, Hetero-Pl-50 and Hetero-Pl-100 configurations with 75 ps plastic time resolution ($Pl-\tau2$). Similar curves were obtained for $Pl-\tau1$ and $Pl-\tau3$.

very similar contrasts but have different detection efficiencies, which heavily influences the propagation of error in the CNR denominator.

IV. Discussion

This paper investigated the potential impact of heterostructured scintillators in PET imaging. We demonstrated the system's CTR improvement with heterostructures, which led to better contrast recovery in early iterations. Also, we saw a substantial loss in sensitivity and the effect of higher complexity in modeling the timing response of these detectors.

The CNR can best summarize the trade-off between timing resolution and effective stopping power discussed in this paper. As shown in Fig. 8, in early iterations, the improvements in convergence keep the heterostructures on par with the BGO-based scanner. However, after the 15th iteration, the BGO-based scanner has a clear lead. Unlike bulk detectors, heterostructures can be configured to optimize the said trade-off, and the tools we developed here can inform such designs.

In the literature, the TOF SNR gain is described as proportional to sensitivity, more specifically to noise equivalent counts [39], and inversely proportional to the timing resolution $1/CTR$ [7], [40]. Thus, if the sensitivity is reduced by introducing the plastic layers to about half of BGO, we should aim for a substantial improvement in CTR to maintain the image's noise properties. However, as discussed later, the PTS (DOI) sets practical limitations on the potential CTR improvement.

The model for the calculation of the timing resolution based on the energy depositions shows that higher energy deposition in the fast plastic scintillator improves the CTR (Fig. 3). Moreover, the simulations showed that larger deposition could

be achieved with thicker plastic layers, which, as mentioned earlier, reduces the detector's effective stopping power.

In the two configurations here, we saw that the fraction of events that deposit some energy in the plastic seems to be independent of the plastic's thickness. The Hetero-Pl-50 offered the best compromise between photon detection efficiency and time resolution.

For the fast emitter to be combined with the dense scintillator, we chose the plastic scintillator EJ232 (Eljen Technology) as it combines a fast signal (rise time below 50 ps) and a high light output (8000-10000 ph/MeV). The properties of EJ232 are very similar to BC422 (Saint-Gobain) that was used by Turtos et al. [21]. Denser than plastic materials could be considered in future heterostructured detector designs that can also have different geometry than stacking layers, like fiber-based designs [26]. An alternative to plastic scintillators can be the nanocrystals [19], [41], [42].

We will add a few specific notes on the image reconstruction for heterostructures. As described earlier, the timing resolution depends on the energy deposition and sharing, leading to a complex TOF model for the scanner. However, here, the variety of timing resolutions obtained from the different combinations of detected events is much wider than in cases investigated previously [27], [43]. Efthimiou *et al.* [27], [43], studying Cherenkov-based detectors [44]–[48], reported that the complexity of the reconstruction with multiple (25) kernels slowed down their convergence. In this work, with only three Gaussian kernels, the Contrast Recovery Coefficient (CRC) converged slightly faster than the single and slower TOF kernel used for the BGO.

Furthermore, the time difference distribution's shape depends on the average DOI of each material and the specific pathway on an event-by-event case [49]. We saw that the above led to a loss in CRC with plastic time resolution near the DOI of the material (51 ps) [34]. Our findings are in agreement with past studies [32], [50]. Also, several groups have proposed the time-walk correction or other methods [45], [51]–[53] to improve the shape of the distribution or account for it with bulk (pixelated or monolithic) crystals. However, heterostructures add another layer of complexity to this.

We should emphasize that the input values for the BGO and the plastic scintillator strongly influence the outcome of this study. The values used here, 271 ps for BGO and 94 ps for plastic, are based on a laboratory setup with high-frequency readout electronics. However, these time resolutions have not yet been used in a full PET system. In the future, we could use CTRs that can be achieved practically at the system level for comparison. Then, the benefits of the heterostructure should become more prominent with a larger difference between the CTR of plastic and BGO.

In the future, we plan to simulate a single detector that includes the optical photons and experimental measurements of a heterostructure with a matrix of 4x4 pixels. The results may lead to the adjustment of our model and input parameters, and the repetition of this simulation study. In addition, the reconstruction model can be optimized to make the best use of the events with very fast time resolution and to study the effects of the heterostructures on the positioning of the events and the spatial resolution.

V. Conclusion

In this paper, we presented the incorporation of a model to calculate the detector's timing resolution based on the deposited energy of each gamma ray in Monte Carlo simulations. This modification allowed us to simulate, for the first time, PET geometries based on heterostructured detectors.

Then, we advanced to reconstruct the simulated data using three TOF kernels and compared the image quality of the said PET detectors to typical BGO. As we showed, the CTR depends on the energies deposited in the different materials of the heterostructured scintillator and the layer sizes. The images presented marginal improvements on contrast recovery and convergence of the algorithm due to the fraction of events with very fast timing resolution. However, introducing the low-density plastic layers strongly reduced the effective stopping power and thus the noise properties of the reconstructed image.

The tools developed here can inform future heterostructure designs on the trade-off between sensitivity and fast time resolution and evaluate their performance.

VI. Acknowledgments

This work received support from the CERN Budget for Knowledge Transfer to Medical Applications. It was initiated in the frame of COST Action TD1401 (FAST) and performed in the frame of the Crystal Clear Collaboration. All authors declare that they have no known conflicts of interest in terms of competing financial interests or personal relationships that could have an influence or are relevant to the work reported in this paper.

References

[1] G. Muehllehner and J. S. Karp, "Positron emission tomography," *Phys. Med. Biol.*, vol. 51, no. 13, R117–R137, Jun. 2006.

[2] C. L. Melcher, "Scintillation Crystals for PET," *J. Nucl. Med.*, vol. 41, no. 6, pp. 1051–1055, Jun. 2000.

[3] D. R. Schaart, G. Schramm, J. Nuyts, and S. Surti, "Time of Flight in Perspective: Instrumental and Computational Aspects of Time Resolution in Positron Emission Tomography," *IEEE Trans. Radiat. Plasma Med. Sci.*, vol. 5, no. 5, pp. 598–618, 2021.

[4] T. Tomitani, "Image Reconstruction and Noise Evaluation in Photon Time-of-Flight Assisted Positron Emission Tomography," *IEEE Trans. Nucl. Sci. 28 4582–9*,

[5] M. Toussaint, R. Lecomte, and J.-P. Dussault, "Improvement of spatial resolution with iterative pet reconstruction using ultrafast tof," *IEEE Trans. Radiat. Plasma Med. Sci*, vol. 5, no. 5, pp. 729–737, 2021.

[6] J. S. Karp, S. Surti, M. E. Daube-Witherspoon, and G. Muehllehner, "Benefit of time-of-flight in PET: experimental and clinical results," *J. Nucl. Med.*, vol. 49, no. 3, pp. 462–470, Mar. 2008. arXiv: NIHMS150003.

[7] M. Conti, "Focus on time-of-flight PET: The benefits of improved time resolution," *Eur. J. Nucl. Med. Mol. Imaging*, vol. 38, no. 6, pp. 1147–1157, Jun. 2011.

[8] M. Conti, L. Eriksson, and V. Westerwoudt, "Estimating Image Quality for Future Generations of TOF PET Scanners," *IEEE Trans. Nucl. Sci.*, vol. 60, Feb. 2013.

[9] M. Conti and B. Bendriem, "The new opportunities for high time resolution clinical TOF PET," *Clin. Transl. Imaging.*, vol. 7, no. 2, pp. 139–147, Apr. 2019.

[10] C. Tsoumpas, "Why ultrafast is ultra-good," *Physics world, 33(6), pp. 41-44*, [Online]. Available: https://physicsworld.com/a/why-ultrafast-detection-is-ultra-good/.

[11] D. R. Schaart, G. Schramm, J. Nuyts, and S. Surti, "Time of flight in perspective: Instrumental and computational aspects of time resolution in positron emission tomography," *IEEE Trans. Radiat. Plasma Med. Sci.*, vol. 5, no. 5, pp. 598–618, 2021.

[12] J. van Sluis *et al.*, "Performance Characteristics of the Digital Biograph Vision PET/CT System," *J. Nucl. Med.*, vol. 60, no. 7, pp. 1031–1036, Jul. 2019.

[13] I. Rausch, A. Ruiz, I. Valverde-Pascual, J. Cal-González, T. Beyer, and I. Carrio, "Performance Evaluation of the Vereos PET/CT System According to the NEMA NU2-2012 Standard," *J. Nucl. Med.*, vol. 60, no. 4, pp. 561–567, Apr. 2019.

[14] S. Niedźwiecki *et al.*, "J-PET: A new technology for the whole-body PET imaging," *Acta Phys. Pol. B*, vol. 48, no. 10, p. 1567, 2017.

[15] P. Moskal *et al.*, "Positronium imaging with the novel multiphoton pet scanner," *Science Advances*, vol. 7, no. 42, eabh4394, 2021.

[16] P. Lecoq, "Metamaterials for novel x- or g-ray detector designs," *2008 IEEE Nucl. Sci. Symp. Conf. Rec.*, vol. N07-1, pp. 680–684,

[17] P. Lecoq, "Pushing the Limits in Time-of-Flight PET Imaging," *IEEE Trans. Radiat. Plasma Med. Sci.*, vol. 1, no. 6, pp. 473–485, Nov. 2017.

[18] Z. Lin, S. Lv, Z. Yang, J. Qiu, and S. Zhou, "Structured scintillators for efficient radiation detection," *Adv. Sci.*, vol. 9, no. 2, p. 2 102 439, 2022.

[19] G. Konstantinou, P. Lecoq, J. M. Benlloch, and A. J. Gonzalez, "Metascintillators for ultrafast gamma detectors: A review of current state and future perspectives," *IEEE Trans. Radiat. Plasma Med. Sci.*, vol. 6, no. 1, pp. 5–15, 2022.

[20] P. Lecoq *et al.*, "Roadmap toward the 10 ps time-of-flight PET challenge," *Phys. Med. Biol.*, vol. 65, no. 21, 21RM01, Oct. 2020.

[21] R. M. Turtos, S. Gundacker, E. Auffray, and P. Lecoq, "Towards a metamaterial approach for fast timing in PET: Experimental proof-of-concept," *Phys. Med. Biol.*, vol. 64, no. 18, p. 185 018, Sep. 2019.

[22] F. Pagano, M. Salomoni, N. Kratochwil, M. Pizzichemi, M. Paganoni, and E. Auffray, "Towards a New Generation of Scintillators in TOF-PET: Heterostructure Scintillator Pixels," *2021 IEEE Nucl. Sci. Symp. Med. Imaging Conf. (NSS/MIC)*,

[23] P. Lecoq *et al.*, "Metascintillators: New results for TOFPET applications," Nov. 2021. [Online]. Available: https://www.techrxiv.org/articles/preprint/Metascintillators_New_results_for_TOFPET_applications/17056166.

[24] F. Pagano, N. Kraotchwil, M. Salomoni, M. Pizzichemi, M. Paganoni, and E. Auffray, "Advances in Heteorostructure Scintillators: Toward a new Generation of Detector for TOF-PET.," *under review in Phys. Med. Biol.*,

[25] F. Loignon-Houle, S. A. Charlebois, R. Fontaine, and R. Lecomte, "Monte carlo simulations of energy, time and spatial evolution of primary electrons generated by 511 kev photons in various scintillators," *Nucl. Instrum. Methods. Phys. Res. A*, vol. 1030, p. 166 449, 2022. [Online]. Available: https://www.sciencedirect.com/science/article/pii/S0168900222000912.

[26] P. Krause *et al.*, "Design Rules for Time of Flight Positron Emission Tomography (ToF-PET) Heterostructure Radiation Detectors.," [Online]. Available: https://ssrn.com/abstract=3966915.

[27] N. Efthimiou *et al.*, "TOF-PET image reconstruction with multiple timing kernels applied on Cherenkov radiation in BGO," *IEEE Trans. Radiat. Plasma Med. Sci.*, vol. 5, pp. 703–711, Dec. 2020.

[28] S. Vandenberghe, E. Mikhaylova, E. D'Hoe, P. Mollet, and J. Karp, "Recent developments in time-of-flight pet," *EJNMMI Physics*, vol. 3, no. 3, 2016.

[29] S. Vinogradov, "Approximations of coincidence time resolution models of scintillator detectors with leading edge discriminator," *Nucl. Instrum. Methods Phys. Res. A: Accel. Spectrom. Detect. Assoc. Equip.*, New Developments In Photodetection 2017, vol. 912, pp. 149–153, Dec. 2018.

[30] S. Gundacker *et al.*, "Experimental time resolution limits of modern SiPMs and TOF-PET detectors exploring different scintillators and Cherenkov emission," *Phys. Med. Biol.*, vol. 65, no. 2, p. 025 001, Jan. 2020.

[31] S. Jan *et al.*, "GATE: A simulation toolkit for PET and SPECT," *Phys. Med. Biol.*, vol. 49, no. 19, pp. 4543–4561, Oct. 2004.

[32] N. Efthimiou, K. Thielemans, E. Emond, C. Cawthorne, S. Archibald, and C. Tsoumpas, "Use of non-Gaussian Time-of-Flight kernels for image reconstruction of Monte Carlo simulated data of ultra-fast PET scanners," *EJNMMI Phys.*, vol. 7, p. 42, Jun. 2020.

[33] National Electrical Manufacturers Association, *Performance Measurements of Positron Emission Tomographs (PET)*, 2012.

[34] N. Efthimiou, E. Emond, P. Wadhwa, C. Cawthorne, C. Tsoumpas, and K. Thielemans, "Implementation and validation of time-of-flight PET image reconstruction module for listmode and sinogram projection data in the STIR library," *Phys. Med. Biol.*, vol. 64, no. 3, p. 035 004, Jan. 2019.

[35] K. Thielemans *et al.*, "STIR: Software for tomographic image reconstruction release 2," *Phys. Med. Biol.*, vol. 57, pp. 867–83, Feb. 2012.

[36] E. Ovtchinnikov *et al.*, "SIRF: Synergistic Image Reconstruction Framework," *Comput. Phys. Commun*, p. 107 087, Dec. 2019.

[37] J. H. Hubbell and S. M. Seltzer, "Tables of X-Ray Mass Attenuation Coefficients and Mass Energy-Absorption Coefficients 1 keV to 20 MeV for Elements Z = 1 to 92 and 48 Additional Substances of Dosimetric Interest," Jan. 1995.

[38] C. Michail *et al.*, "A novel method for the optimization of positron emission tomography scanners imaging performance," *Hell. J. Nucl. Med.*, vol. 19, no. 3, pp. 231–240, Sep. 2016.

[39] S. Strother, M. Casey, and E. Hoffman, "Measuring PET scanner sensitivity: Relating countrates to image signal-to-noise ratios using noise equivalent counts," *Nuclear Science, IEEE Transactions on*, vol. 37, pp. 783–788, May 1990.

[40] D. R. Schaart, "Physics and technology of time-of-flight PET detectors," *Phys. Med. Biol.*, vol. 66, no. 9, 09TR01, Apr. 2021.

[41] R. M. Turtos *et al.*, "On the use of CdSe scintillating nanoplatelets as time taggers for high-energy gamma detection," *npj 2D Mater Appl*, vol. 3, no. 1, pp. 1–10, Oct. 2019.

[42] K. Tomanová *et al.*, "On the structure, synthesis, and characterization of ultrafast blue-emitting CsPbBr3 nanoplatelets," *APL Mat.*, 011104, 2019.

[43] N. Efthimiou *et al.*, "Time-Of-Flight PET Image Reconstruction with Complex Timing Kernels: The Case of BGO Cherenkov Photons," in *2020 IEEE Nucl. Sci. Symp. Med. Imaging Conf. (NSS/MIC)*, IEEE, pp. 1–4.

[44] S. E. Brunner and D. R. Schaart, "BGO as a hybrid scintillator / Cherenkov radiator for cost-effective time-of-flight PET," *Phys. Med. Biol.*, vol. 62, no. 11, pp. 4421–4439, Jun. 2017.

[45] N. Kratochwil, S. Gundacker, P. Lecoq, and E. Auffray, "Pushing Cherenkov PET with BGO via coincidence time resolution classification and correction," *Phys. Med. Biol.*, vol. 65, no. 11, p. 115 004, Jun. 2020.

[46] G. Ariño-Estrada *et al.*, "Study of Čerenkov Light Emission in the Semiconductors TlBr and TlCl for TOF-PET," *IEEE Trans. Radiat. Plasma Med. Sci.*, vol. 5, no. 5, pp. 630–637, 2021.

[47] G. Terragni *et al.*, "Time Resolution Studies of Thallium Based Cherenkov Semiconductors," *Front. Phys.*, vol. 10, 2022.

[48] A. Gonzalez-Montoro, S. Pourashraf, J. W. Cates, and C. S. Levin, "Cherenkov Radiation–Based Coincidence Time Resolution Measurements in BGO Scintillators," *Front. Phys.*, vol. 10, 2022.

[49] M. Toussaint, F. Loignon-Houle, J.-P. Dussault, and R. Lecomte, "Analytical model of DOI-induced time bias in ultra-fast scintillation detectors for TOF-PET," *Phys. Med. Biol.*, vol. 64, no. 6, p. 065 009, Mar. 2019.

[50] M. E. Daube-Witherspoon, S. Surti, S. Matej, M. Werner, S. Jayanthi, and J. S. Karp, "Influence of Time-of-Flight Kernel Accuracy in TOF-PET Reconstruction," in *2006 IEEE Nucl. Sci. Symp. Conf. Rec.*, vol. 3, pp. 1723–1727.

[51] M. Pizzichemi *et al.*, "On light sharing TOF-PET modules with depth of interaction and 157 ps FWHM coincidence time resolution," *Phys. Med. Biol.*, vol. 64, no. 15, p. 155 008, Aug. 2019.

[52] J. Du, G. Ariño-Estrada, X. Bai, and S. R. Cherry, "Performance comparison of dual-ended readout depth-encoding PET detectors based on BGO and LYSO crystals," *Phys. Med. Biol.*, vol. 65, no. 23, p. 235 030, Nov. 2020.

[53] F. Loignon-Houle *et al.*, "DOI estimation through signal arrival time distribution: A theoretical description including proof of concept measurements," *Phys. Med. Biol.*, vol. 66, no. 9, p. 095 015, Apr. 2021.